ACS APPLIED MATERIALS & INTERFACES

www.acsami.org Research Article

Enhanced Electrical Conductivity and Mechanical Properties of Stretchable Thermoelectric Generators Formed by Doped Semiconducting Polymer/Elastomer Blends

Yun Chang,[§] Yi-Hsuan Huang, Po-Shen Lin, Shao-Huan Hong, Shih-Huang Tung, and Cheng-Liang Liu*

Cite This: *ACS Appl. Mater. Interfaces* 2024, 16, 3764−3777 Read Online

ACCESS | Metrics & More | Article Recommendations | Supporting Information

ABSTRACT: Recent research efforts have concentrated on the development of flexible and stretchable thermoelectric (TE) materials. However, significant challenges have emerged, including increased resistance and reduced electrical conductivity when subjected to strain. To address these issues, rigid semiconducting polymers and elastic insulating polymers have been incorporated and nanoconfinement effects have been exploited to enhance the charge mobility. Herein, a feasible approach is presented for fabricating stretchable TE materials by using a doped semiconducting polymer blend consisting of either poly(3-hexylthiophene) (**P3HT**) or poly(3,6-dithiophen-2-yl-2,5-di(2-decyltetradecyl)-pyrrolo[3,4-*c*]pyrrole-1,4-dione-*alt*-thienylenevinylene-2,5-yl) (**PDVT-10**) as the rigid polymer with styrene-ethylene-butylene-styrene (**SEBS**) as the elastic polymer. In particular, the blend composition is optimized to achieve a continuous network structure with **SEBS**, thereby improving the stretchability. The optimized polymer films exhibit well-ordered microstructural aggregates, indicative of good miscibility with $FeCl_3$ and enhanced doping efficiency. Notably, a lower activation energy and higher charge-carrier concentration contribute to an improved electrical conductivity under high tensile strain, with a maximum output power of 1.39 nW at a ΔT of 22.4 K. These findings offer valuable insights and serve as guidelines for the development of stretchable p−n junction thermoelectric generators based on doped semiconducting polymer blends with potential applications in wearable electronics and energy harvesting.

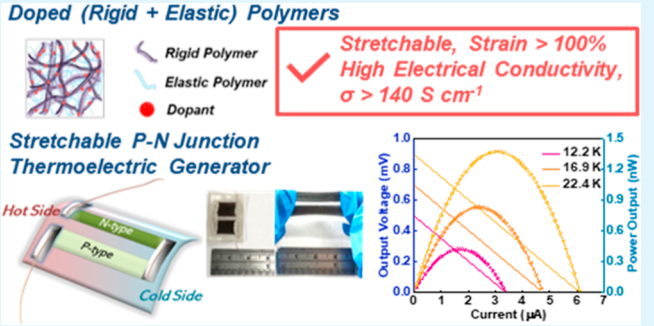

KEYWORDS: *organic thermoelectrics, polymer blends, conjugated polymers, donor−acceptor, doping, stretchable*

INTRODUCTION

Thermoelectric (TE) effects involve an interplay between thermal and electrical phenomena and offer a unique capability to directly convert heat into electricity. With the growing global emphasis on sustainable energy sources, these effects have gained significant attention in recent years.[1−5] The fundamental principle governing TE phenomena is the Seebeck effect, whereby a considerable number of electrons concurrently carry both heat and electricity in an equilibrium state. This enables the transfer of electrons from a region of higher temperature to a region of lower temperature, thereby resulting in a potential difference across the TE material. This principle has been exploited in the development of organic thermoelectric generators (TEGs), which facilitate the direct conversion of thermal energy into electricity.[4,6] Over the course of more than six decades of productive research, organic TE materials have demonstrated successful applications in diverse areas such as the conversion of solar energy, radioisotope energy, automotive waste heat, and industrial heat into electricity. Additionally, the generated electricity can be used to operate TE devices, such as solid-state heat pumps for distributed refrigeration. The recent surge in the market for wearable electronics and the advent of internet of things (IoT) technology have spurred a pronounced interest in TEGs due to their potential use as long-lasting, portable, and maintenance-free power sources.[7] These devices hold immense promise in leveraging the temperature differential between the human body and the environment as a heat source for powering low-power wearable electronics and realizing self-powered systems. Furthermore, TE-based devices are emerging as integral components of IoT sensors for monitoring extreme environmental temperatures, or the body temperature in healthcare

Received: October 19, 2023
Revised: December 26, 2023
Accepted: December 29, 2023
Published: January 16, 2024

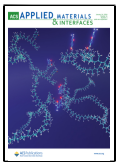

https://doi.org/10.1021/acsami.3c15651
ACS Appl. Mater. Interfaces 2024, 16, 3764−3777

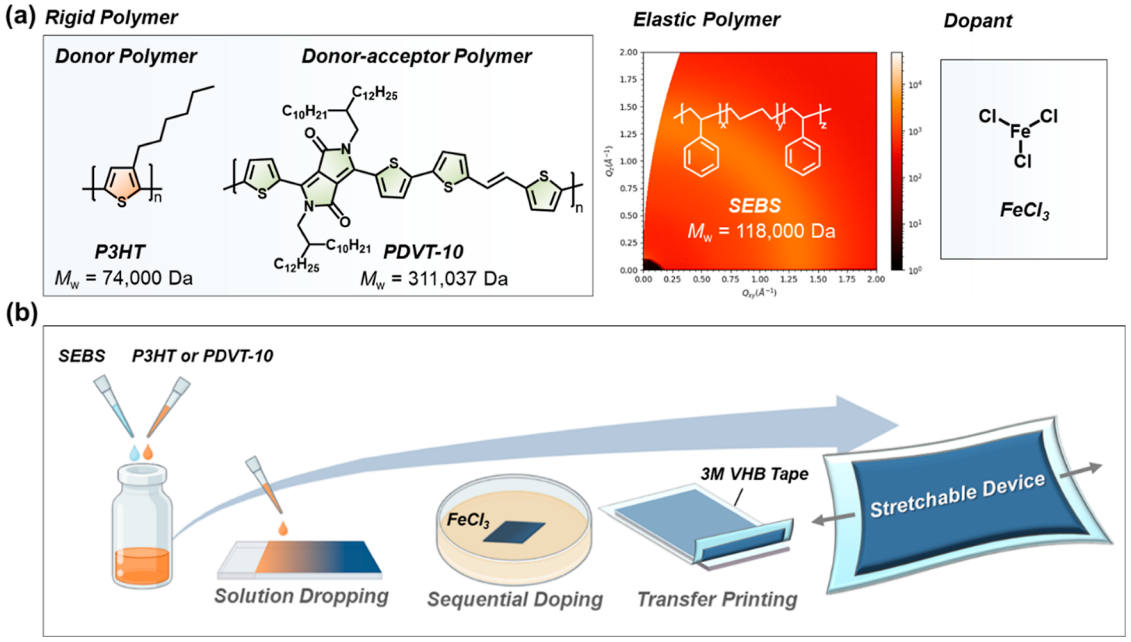

Figure 1. (a) Molecular structures of rigid polymers (**P3HT** and **PDVT-10**), elastic polymer (**SEBS**), and dopant ($FeCl_3$). (b) The fabrication process of stretchable doped semiconducting polymer blend TE film.

settings, and providing tactile sensory feedback in human-machine interaction applications.[8−11]

The performance of wearable and stretchable TE devices critically relies on achieving a delicate balance between the electrical conductivity and the Seebeck coefficient. While a high electrical conductivity is essential for efficient charge transport, an appropriate Seebeck coefficient is crucial for generating a significant TE effect. This challenge becomes even more pronounced in wearable applications, where mechanical deformations and strains can significantly alter the material properties.[12−14] Consequently, the selection of appropriate components assumes paramount importance, with the incorporation of rigid semiconducting polymers and elastic insulating polymers playing a critical role in achieving the desired properties. For example, Kiefer et al. sequentially doped a blend of stretchable polymer semiconductors and elastomers to achieve an impressive stretchability of up to 100% strain, but this was accompanied by a significant increase in resistance, which posed challenges for achieving optimal TE performance.[15] Meanwhile, Jeong et al. focused on maintaining a stable TE performance under strains of up to 100%, but at the expense of a relatively low electrical conductivity.[16] Hence, the development of wearable TE devices necessitates innovative approaches to optimizing both the electrical conductivity and the Seebeck coefficient, while ensuring mechanical flexibility and durability. For example, Xu et al. studied the use of blends of diketopyrrolopyrrole (**DPP**)-based donor−acceptor polymers with the thermoplastic elastomer styrene-ethylene-butylene-styrene (**SEBS**) in organic field-effect transistor applications.[17,18] By leveraging the nano-confinement effect, these researchers were able to enhance and sustain electron mobility even under high strains, thereby sparking interest in the potential of these blends as TE materials. In addition, the commonly used semiconducting polymer poly(3-hexylthiophene) (**P3HT**) is compatible with elastomers, thus allowing for the creation of stretchable blends without compromising the electrical properties, while ferric chloride ($FeCl_3$) has emerged as a popular dopant for TE materials due to its high doping efficiency.[19−31] By combining these various components and harnessing their unique properties, researchers have identified a promising pathway for the development of stretchable TE devices with improved performance, flexibility, and adaptability. These recent advancements in TE materials hold significant implications for the realization of innovative, self-powered electronic systems capable of withstanding challenging environmental conditions.

In the present study, stretchable TE materials are fabricated by utilizing novel blends of either poly(3-hexylthiophene) (**P3HT**) as the rigid donor polymer, or poly(3,6-dithiophen-2-yl-2,5-di(2-decyltetradecyl)-pyrrolo[3,4-*c*]pyrrole-1,4-dione-*alt*-thienylenevinylene-2,5-yl) (**PDVT-10**) as the rigid donor−acceptor polymer, with the elastic polymer styrene-ethylene-butylene-styrene (**SEBS**) to improve the stretchability of the resulting TE materials. In addition, the doping component $FeCl_3$ is used to improve the electrical properties of the blends. The primary aim of this study is to optimize the composition of the polymer blend and establish a continuous network structure with **SEBS** in order to enhance the stretchability of the TE material. The resulting polymer films exhibit a distinctive fiber-like morphology and microstructurally ordered aggregates, thereby indicating good miscibility between each polymer and $FeCl_3$, while achieving a higher doping efficiency. The combination of a lower activation energy and a higher number density of charge carriers results in an improved electrical conductivity, even under conditions of high tensile strain. The present results offer valuable insights and practical guidelines for the development of stretchable p−n junction TEGs using doped semiconducting polymer blends with significant implications for potential applications in wearable electronics and energy harvesting.

EXPERIMENTAL SECTION

Sample Preparation. The molecular structures of the samples are shown in Figure 1a. These include the rigid polymers **P3HT** (M_w =

https://doi.org/10.1021/acsami.3c15651
ACS Appl. Mater. Interfaces 2024, 16, 3764−3777

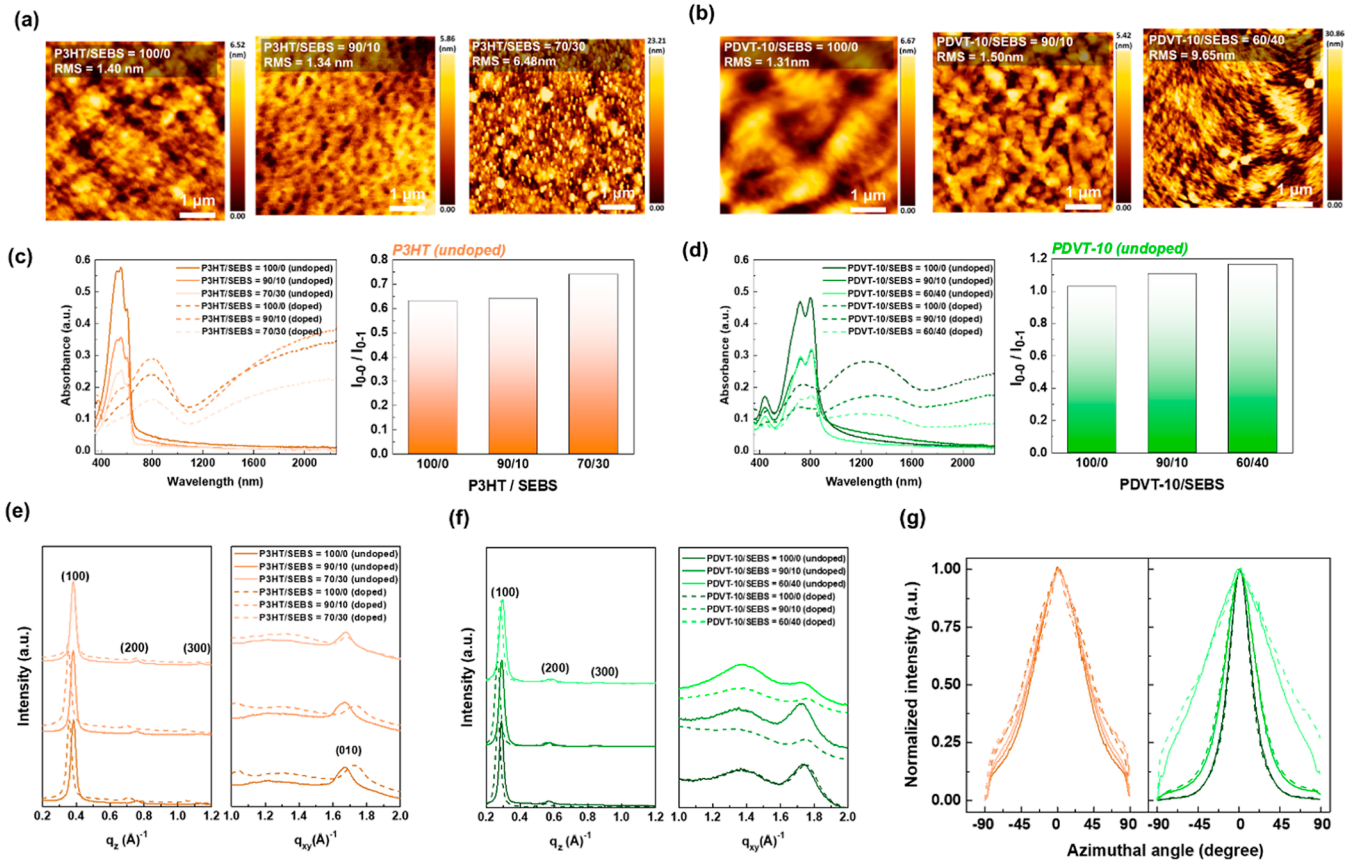

Figure 2. AFM height images of undoped (a) **P3HT**/**SEBS** = 100/0, 90/10, 70/30 and (b) **PDVT-10**/**SEBS** = 100/0, 90/10, 60/40 blend films. UV−vis−NIR absorbance spectra and I_{0-0}/I_{0-1} for undoped and doped (c) **P3HT**/**SEBS** = 100/0, 90/10, 70/30, and (d) **PDVT-10**/**SEBS** = 100/0, 90/10, 60/40 blend films. Line-cut profiles from the GIWAXS measurements, (100) from out of plane direction and (010) from in plane direction for undoped and doped (e) **P3HT**/**SEBS** = 100/0, 90/10, 70/30 and (f) **PDVT-10**/**SEBS** = 100/0, 90/10, 60/40 blend films. (g) Azimuthal angle of (100) peak diffraction for undoped and doped for undoped and doped **P3HT**/**SEBS** = 100/0, 90/10, 70/30 and **PDVT-10**/**SEBS** = 100/0, 90/10, 60/40 blend films.

74,000 Da) and **PDVT-10** (M_w = 311,037 Da), along with the thermoplastic elastomer, **SEBS**, and the $FeCl_3$ dopant. Each rigid polymer was combined with **SEBS** in order to elucidate the influence of intermolecular interactions between the rigid polymer domains on the connectivity within the elastic polymer matrix. The rigid and elastic polymer blends were prepared by mixing the respective solutions in a 7:3 chloroform/1,2-dichlorobenzene solvent (10 mg mL^{-1}) to achieve the desired weight fractions of rigid polymer/elastic polymer ranging from 100/0 to 0/100. Subsequently, the polymer blend solution was then drop-cast onto an octadecyltrichlorosilane (ODTS)-treated glass substrate at 70 °C for 20 min, followed by annealing at 190 °C for 15 min inside a nitrogen-filled glovebox. The doping procedure involved immersing the polymer blend films in a 5 mg mL^{-1} $FeCl_3$/acetonitrile solution for 1 min. As shown in Figure 1b, the doped polymer blend films were then transferred onto 3M VHB tape to serve as the stretchable TE device. The film thicknesses were approximately 2 μm, as determined by using an alpha-step IQ profilometer (KLA-Tencor). Thickness reliability was ensured through a minimum of three measurements for each film device, followed by the calculation of the average value. The TE parameters of doped polymer thin film samples, including the Seebeck coefficient and electrical conductivity, were simultaneously measured using a commercial ZEM-3 measurement system (ADVANCE RIKO Inc., Japan) at 303 K with three different temperature gradients under a helium atmosphere. The electrical conductivity (σ) was determined from the resistance (R), width (w), thickness (t), and length (l) of the sample, as expressed by eq 1

$$\sigma = \frac{l}{Rwt} \tag{1}$$

Fabrication of a Stretchable p−n Junction TEG. The fabrication process involved drop-casting a 90/10 **PDVT-10**/**SEBS** solution onto an ODTS-treated glass substrate. The p-type and n-type doping processes involved immersing the blend films in a 5 mg mL^{-1} $FeCl_3$/acetonitrile solution for 5 min to achieve p-type doping and an 81 mg mL^{-1} $FeCl_3$/acetonitrile solution for 5 min for n-type, as well. After doping, the p- and n-doped blend films were transferred onto distinct sections of 3M VHB tape and connected using copper wires and silver conducting pastes. To ensure stability of TEG, it was carefully encapsulated by applying tape on the top side within a nitrogen-filled glovebox. This step was taken to mitigate the sensitivity of the $FeCl_3$-doped films to exposure to ambient air. The measurement setup employed two Peltier units, each serving as separate stage to maintain temperature differences. These units functioned as the hot and cold sides independently. The temperatures at both ends of the TEGs, which were coated with silver paste, were monitored using two thermocouples. The measurements were performed using a Keithley 2400 source meter, a Keithley 2182A nanovoltmeter, and a Keithley DAQ6510 data acquisition/logging multimeter system.

RESULTS AND DISCUSSION

Selective Reason of Rigid/Elastic Polymers. The rigid polymers **P3HT** (M_w = 74,000 Da) and **PDVT-10** (M_w = 311,037 Da), along with the thermoplastic elastomer, **SEBS**, were selected based on the phase separation behaviors of the

https://doi.org/10.1021/acsami.3c15651
ACS Appl. Mater. Interfaces 2024, 16, 3764−3777

rigid/elastic polymer blend materials, and the enthalpic interactions between their respective components were evaluated according to the Flory–Huggins interaction parameter (χ).[32,33] As shown in Table S1 and Figure S1 of the Supporting Information, the calculated χ values for the interactions between the rigid donor polymer (**P3HT**) and the elastic polymer **SEBS**, and between the rigid donor-acceptor polymer (**PDVT-10**) and **SEBS** are 1.76 and 1.99 K, respectively, thereby suggesting good miscibility of each polymer with **SEBS**.[34] Thus, **SEBS** was selected as the elastic polymer component due to its nonpolar nature and nanoconfinement capability, which effectively reduce its molecular interactions with the rigid polymer component, thereby minimizing the degradation of charge carrier mobility. Furthermore, the addition of **SEBS** to the rigid polymer may induce changes in the thermodynamic and kinetic properties, such as decreasing the Young's modulus and glass transition temperature, and increasing the ductility.[35] Moreover, the presence of **SEBS** contributes to the deformability of the polymer blend, as evidenced by its amorphous halo properties observed in the grazing-incidence wide-angle X-ray scattering (GIWAXS) results (Figure 1a).

Morphological, Optical, and Microstructural Properties of the Blends. The phase-separated structures of the rigid and elastic polymers in the blend system are critical for determining the physical and charge transport properties. Specifically, the following two distinct morphologies can be observed in rigid/elastic polymer blend films based on the dispersion of rigid polymer domains: (i) a continuously connected rigid polymer morphology and (ii) an island-structured rigid polymer morphology. The formation of each morphology is governed by the presence or absence of strong interchain coupling between rigid polymer domains. The continuously connected rigid polymer morphology is highly desirable, as it facilitates efficient charge transport by effectively dispersing and interconnecting rigid polymer domains throughout the elastic polymer domains. By contrast, the island-structured rigid polymer morphology occurs when individual rigid polymer domains are physically separated, often due to the addition of a large amount of elastic polymer. This island-like structure restricts the movement of charge carriers and hinders the charge transport properties.[36,37]

The morphological characteristics of the various as-prepared rigid/elastic polymer blends are revealed by the atomic force microscopy (AFM) and scanning electron microscopy (SEM) results in Figures 2a,b, S2, and S3. Thus, the pristine rigid polymer films (**P3HT**/**SEBS** = 100/0 and **PDVT-10**/**SEBS** = 100/0) exhibit uniform fiber-like morphologies, whereas the polymer blend films clearly exhibit phase separation between the rigid and elastic polymer components due to the intermolecular interactions between each rigid polymer and the **SEBS**. Moreover, when the added fraction of **SEBS** is small (e.g., **P3HT**/**SEBS** = 90/10 and **PDVT-10**/**SEBS** = 90/10), where a small fraction of **SEBS** was added, an intriguing observation was made. The inclusion of **SEBS** facilitated the formation of a continuously connected rigid polymer network facilitated by a nanoconfinement effect, thereby indicating a strong interaction between each rigid polymer and the elastomer. Furthermore, the films with **P3HT**/**SEBS** or **PDVT-10**/**SEBS** ratios of 100/0 and 90/10 all exhibit relatively smooth surfaces with root-mean-square roughness (R_{rms}) values ranging from 1.31 to 1.50 nm (Figure 2a). Nevertheless, small granular aggregates, measuring tens of nanometers in size, are distributed across the surfaces of these samples (Figure 2a,b), and these become more prominent as the **SEBS** ratio is increased (**P3HT**/**SEBS** = 70/30 and **PDVT-10**/**SEBS** = 60/40), thereby resulting in the formation of island-like rigid polymer morphologies. This can be attributed to phase separation in the presence of the increased amount of **SEBS**.[38−41]

The aggregation strengths of the **P3HT** and **PDVT-10** in the presence or absence of **SEBS** are elucidated by the ultraviolet–visible–near-infrared (UV–vis–NIR) absorbance spectra in the solution and film states in Figure 2c,d and in Figure S4. Thus, in each type of polymer, the addition of **SEBS** results in a decrease in the intensity of the absorption peak for the rigid polymer, indicating the contribution of **SEBS** to the overall transmittance. For donor polymer **P3HT** and its blends, a significant shift in the absorption peak is observed, from ∼456 nm in the solution state to ∼555 nm in the film state, thus suggesting a distinct alteration in the molecular arrangement upon film formation. By contrast, the absorption peaks of the donor–acceptor polymer **PDVT-10** and its blends exhibit minimal shifts between the solution and film states, thus suggesting the presence of preaggregation and strong intermolecular interactions even in the solution phase of **PDVT-10**.[18,36,42,43]

Further insights into the effects of **SEBS** addition are provided by an analysis of the intensity ratio of the I_{0-0} and I_{0-1} peaks obtained from the normalized absorbances of the blend films in Figure S4. Specifically, the higher I_{0-0}/I_{0-1} peak ratios of the blend films compared to the pristine **P3HT** and **PDVT-10** films clearly indicate the increased interactions between the rigid polymer chains and/or improved backbone planarity within the blend films. Upon the addition of **SEBS**, phase separation occurs, leading to the formation of rigid polymer microdomains in contact with the **SEBS** phases. As a result, the **P3HT** or **PDVT-10** chains can become regularly arranged along the interfaces between the microdomains and the matrix to provide a more ordered polymer crystalline packing, thereby strengthening the intramolecular interactions. This combination of phase separation and enhanced intramolecular interactions contributes to the observed higher I_{0-0}/I_{0-1} peak ratios of the blend films. Moreover, the **PDVT-10**/**SEBS** films exhibit higher I_{0-0}/I_{0-1} peak ratios than the **P3HT**/**SEBS** films, thus suggesting the presence of enhanced molecular interactions within the donor–acceptor polymer system.[44]

The effects of $FeCl_3$ doping on the polymer blends are also revealed by the results in Figure 2c,d. Thus, while the undoped films exhibit no significant absorbance beyond 1000 nm, a decrease in the absorption intensity of each neutral polymer is observed along with the appearance of new absorbance bands in the NIR region (above 1000 nm) after doping with $FeCl_3$. The latter absorption bands are attributed to the generation of (bi)polaronic species, thereby indicating the occurrence of charge transfer between the polymer and the dopant.

The molecular arrangements and crystallinities of the polymer blend films, along with the effects of doping, are further elucidated by the GIWAXS results in Figure 2e,f, and in Figures S5 and S6. Furthermore, the line-cut profiles from Figure 2e,f were used to determine the lamellar spacing ($d_{(100)}$) in the q_z direction and the $\pi-\pi$ spacing ($d_{(010)}$) in the q_{xy} direction, the results of which are summarized in Table S2. In the case of the undoped **P3HT**/**SEBS** blends with compositions ranging from 100/0 to 60/40, the ring-like

https://doi.org/10.1021/acsami.3c15651
ACS Appl. Mater. Interfaces 2024, 16, 3764−3777

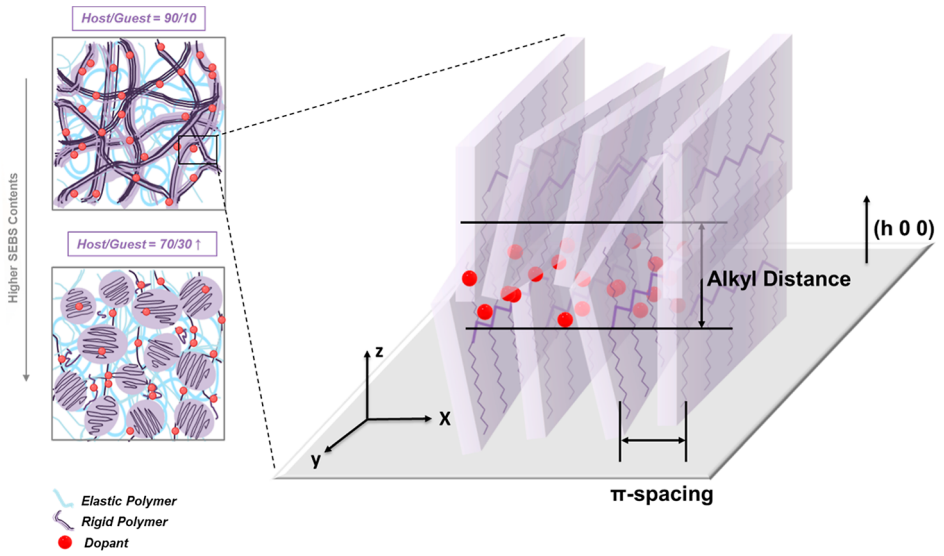

Figure 3. Schematic diagram illustrates the influence of **SEBS** and $FeCl_3$ on the morphologies of doped rigid/elastic Polymer blend films containing low (90/10) and high SEBS contents (**SEBS** contents more than 30 wt %). Additionally, the diagram depicts the effect of $FeCl_3$ doping on the crystalline structure of rigid/elastic polymer = 90/10 films.

GIWAXS diffraction patterns suggest the presence of fewer oriented crystallites, and the incorporation of **SEBS** does not disrupt the crystalline structure of **P3HT**. By contrast, the undoped pristine **PDVT-10** film exhibits lamellar stacking reflections (h00) primarily in the q_z direction, thereby indicating a predominant edge-on orientation, while the addition of **SEBS** results in fewer edge-on oriented crystallites and the appearance of an amorphous halo due to the **SEBS** component. Meanwhile, distinct (100), (200), (300), and (010) diffraction patterns are observed in the doped and undoped samples according to varying **SEBS** contents. Thus, the undoped **P3HT/SEBS** blend films each exhibit (100) diffraction peaks at approximately 0.38 $Å^{-1}$ in the q_z direction, with a $d_{(100)}$ of 1.65 nm, along with (010) diffraction peaks at approximately 1.67 $Å^{-1}$ in the q_{xy} direction, with a $d_{(010)}$ of 0.38 nm. Similarly, the undoped **PDVT-10/SEBS** blend films exhibit (100) diffraction at 0.30 $Å^{-1}$ in the q_z direction, with a $d_{(100)}$ of 2.13 nm, and (010) diffraction peaks at 1.73 $Å^{-1}$ in the q_{xy} direction, with a $d_{(010)}$ of 0.36 nm. These results are consistent with previous studies of **P3HT** and **PDVT-10** using GIWAXS analysis. After doping, the $d_{(100)}$ values of the 100/0 and 90/10 **P3HT/SEBS** films are found to have increased to 1.76 and 1.78 nm, respectively, while the $d_{(010)}$ has decreased to 0.36 nm and 0.35 Å, respectively. Similarly, in the doped 100/0 and 90/10 **PDVT-10/SEBS** films, the $d_{(100)}$ has increased to 2.21 and 2.25 nm, respectively, while the $d_{(010)}$ has decreased to 0.35 Å in both cases. The observed decrease in $d_{(010)}$ after doping is particularly significant as it indicates a shorter distance between the rigid polymer chains.[45−47]

Further insights on the crystalline morphology are provided by the analysis of the azimuthal full-width-at-half-maximum (FWHM) values of the (100) Bragg sheet in Figure 2g. Here, the **P3HT/SEBS** films with compositions of 100/0, 90/10, and 70/30 exhibit similar FWHM values of ∼72.75, 75.76, and 80.26°, respectively, whereas the FWHM values of the **PDVT-10/SEBS** blends are found to increase significantly from 28.3° for the 100/0 film, through 42.89° for the 90/10 film, and 92.0° for the 60/40 film. This indicates substantial changes in the microstructural characteristics of the **PDVT-10/SEBS** blends, and suggests the presence of a higher fraction of face-on orientation in the **PDVT-10/SEBS** = 60/40 blends than in the pristine **PDVT-10**. Additionally, the **PDVT-10/SEBS** blends exhibit an amorphous broad peak at around 1.37 $Å^{-1}$ in the q_{xy} direction, as observed in the line-cut profiles of Figure 2e,f. Taken together, these observations highlight the influence of **SEBS** on the orientation and crystallinity, with the **PDVT-10** being more susceptible than the **P3HT**.[19,22,48]

Based on the above results, the effects of **SEBS** and $FeCl_3$ on the morphologies of the rigid/elastic polymer blend films are shown schematically in Figure 3. Thus, due to the stronger ion-π interactions, the $FeCl_3$ dopant is thought to be preferentially intercalated between the backbones and side chains of the rigid polymer phase. Consequently, due to the incompatibility between the hydrophobic side chains and the $FeCl_3$, the originally coiled side chains can straighten out and pack more closely, thereby increasing the $d_{(100)}$ and decreasing the $d_{(010)}$, respectively.[22,49,50] In particular, the lower $d_{(010)}$ value plays a crucial role in enhancing the electronic properties of the blended films by improving the charge carrier mobility, thereby facilitating efficient charge transport. However, when the **SEBS** content is further increased, the $d_{(100)}$ and $d_{(010)}$ values of the doped and undoped films **P3HT/SEBS** = 70/30 and **PDVT-10/SEBS** = 60/40 films are unchanged. This may be due to the lower amounts of $FeCl_3$ in the films at higher fractions of **SEBS**, or to the distribution of more $FeCl_3$ dopants in the larger **SEBS** area, as depicted in Figure 3. Consequently, the blends with higher **SEBS** content show weaker charge transport compared to the films with 10 wt % **SEBS**. In brief, the above findings provide valuable insights into the microstructural changes induced by $FeCl_3$ doping, and highlight the role of a reduced $d_{(010)}$ in enhancing the electronic properties of the blend films.[51]

Thermoelectric Performances of the Doped Polymer Blend Films. To examine the doping efficiency and impact of the $FeCl_3$-doped donor and donor−acceptor polymers with various concentrations of **SEBS**, the average electrical conductivities, Seebeck coefficients, and power factors (PF) were measured for at least 10 individual TE devices of each film composition. The results are plotted along with the error bars in Figure 4a−c. Here, the electrical conductivity of the

https://doi.org/10.1021/acsami.3c15651
ACS Appl. Mater. Interfaces 2024, 16, 3764−3777

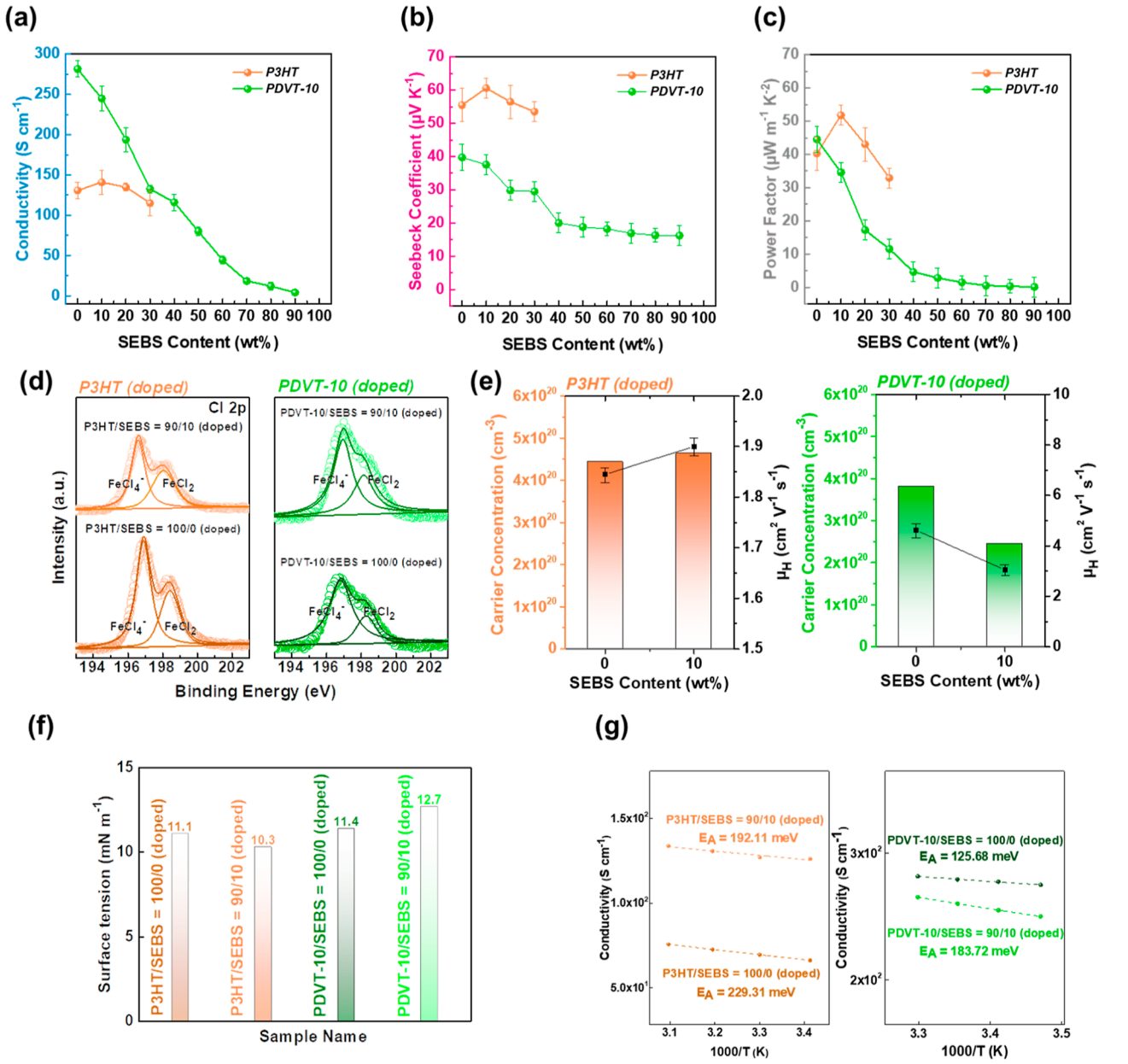

Figure 4. (a) σ, (b) S, and (c) PF for doped **P3HT**/**SEBS** = 100/0 to 70/30, and **PDVT-10**/**SEBS** = 100/0 to 10/90 blend films. (d) XPS spectra of the Cl 2p signal for doped **P3HT**/**SEBS** = 100/0, 90/10, and **PDVT-10**/**SEBS** = 100/0, 90/10 blend films. (e) n and μ_{Hall} measured by Hall effect for doped **P3HT**/**SEBS** = 100/0, 90/10 and **PDVT-10**/**SEBS** = 100/0, 90/10 blend films. (f) Surface tensions measured by contact angle measurement for doped **P3HT**/**SEBS** = 100/0, 90/10 and **PDVT-10**/**SEBS** = 100/0, 90/10 blend films. (g) Temperature dependence of σ and calculated E_A for doped **P3HT**/**SEBS** = 100/0, 90/10, and **PDVT-10**/**SEBS** = 100/0, 90/10 blend films.

doped **P3HT**-based film exhibits an initial increase with the addition of **SEBS**, the doped **P3HT**/**SEBS** = 90/10 blend film (140.9 S cm^{-1}) compared to the doped **P3HT** film (130.7 S cm^{-1}). However, this is followed by a steady decrease in electrical conductivity as the **SEBS** content is increased, giving values that the doped **P3HT**/**SEBS** = 80/20 film exhibited a σ of 134.9 S cm^{-1}, and the doped **P3HT**/**SEBS** = 70/30 film displayed a σ of 114.9 S cm^{-1}. Beyond that, the electrical resistance has increased so dramatically that the TE performance is unmeasurable. These results demonstrate that while a high concentration of **SEBS** disrupts the charge-carrier transport pathway, the addition of **SEBS** at concentrations of less than 40 wt % has minimal impact on the crystallinity and molecular alignment of **P3HT** (see also Figures S5 and S6).

By contrast, the electrical conductivity of the doped **PDVT-10**/**SEBS** blend films immediately decreases with the addition of **SEBS**, from 281.6 S cm^{-1} for the pristine film to 244.9 S cm^{-1} for the **PDVT-10**/**SEBS** = 90/10 film. Moreover, this decrease continues with a further increase in **SEBS** concentration, giving conductivities of 193.9, 132.7, 115.9, 80.0, 44.3, 18.3, 12.0, and 4.03 S cm^{-1} for the 80/20, 70/30, 60/40, 50/50, 40/60, 30/70, 20/80, and 10/90 **PDVT-10**/**SEBS** films, respectively. Nevertheless, the electrical conductivity remains measurable with the addition of up to 90 wt % **SEBS** in the **PDVT-10**-based films, which may be due to the high molecular weight (M_n) of **PDVT-10**, which indicates the presence of long conjugated chains that can limit the disturbance to the charge-carrier transport pathway. Overall,

https://doi.org/10.1021/acsami.3c15651
ACS Appl. Mater. Interfaces 2024, 16, 3764−3777

based on the above trends, the electrical conductivities of the various films decrease in the order: **PDVT-10/SEB** = 100/0 > **PDVT-10/SEBS** = 90/10 > **P3HT/SEBS** = 90/10 > **P3HT/SEBS** = 100/0.

Similar trends are observed in the Seebeck coefficients of the doped **P3HT/SEBS** and **PDVT-10/SEBS** films (Figure 4a–c). Thus, the doped 100/0, 90/10, 80/20, and 70/30 **P3HT/SEBS** films exhibit Seebeck coefficients of 55.5, 60.6, 56.5, and 53.5 μV K^{-1}, respectively, while the Seebeck coefficients of the 100/0, 90/10, 80/20, 70/30, 60/40, 50/50, 40/60, 30/70, 20/80, and 10/90 **PDVT-10/SEBS** films are 39.8, 37.6, 29.8, 29.5, 20.0, 18.8, 18.2, 16.9, 16.3, and 16.2 μV K^{-1}, respectively.

Consistently, the *PF* values of the 100/0, 90/10, 80/20, and 70/30 **P3HT/SEBS** films are 40.3, 51.8, 43.0, and 32.9 μW m^{-1} K^{-1}, respectively, while those of the 100/0, 90/10, 80/20, 70/30, 60/40, 50/50, 40/60, 30/70, 20/80, and 10/90 **PDVT-10/SEBS** films are 44.5, 34.6, 17.2, 11.5, 4.6, 2.8, 1.5, 0.5, 0.3, and 0.1 μW m^{-1} K^{-2}, respectively. These results highlight the significant effect of the **SEBS** blend ratio on the power generation capabilities of TE devices fabricated by using the **P3HT**- and **PDVT-10**-based blends of the TE device. Hence, to gain a deeper understanding of the underlying mechanisms and potential applications of the optimal blend ratio in the fabrication of stretchable TEGs, the following investigations examine the doping efficiency, charge-carrier transport, and stretchability of the films containing 0 and 10 wt % **SEBS** only.

The doping efficiencies of $FeCl_3$ in the **P3HT/SEBS** and **PDVT-10/SEBS** films are revealed by the Gaussian fitting analysis of the X-ray photoelectron spectra (XPS) in the binding energy range of 194–202 eV, where the Cl peak is observed (Figure 4d). In each case, the Cl peak is deconvoluted into two distinct peaks at 197 and 199 eV, corresponding to the presence of $FeCl_4^-$ and $FeCl_2$, respectively, in the doped samples. When the $FeCl_3$ is dissolved in acetonitrile $FeCl_4^-$ and $FeCl_2^+$ ions are formed via the following reactions

$$FeCl_3 \rightarrow FeCl_{4^-} + FeCl_{2^+}$$

and

$$RP + FeCl_{4^-} + FeCl_{2^+} \rightarrow \mathbf{RP}^+ + FeCl_{4^-} + FeCl_2$$

where **RP** indicates the rigid polymer. These $FeCl_2^+$ ions become intercalated between the rigid polymer chains, and electrons are then transferred from the rigid polymer to $FeCl_2^+$ to result in the generation of positive charges on the rigid polymer. This process creates electron-deficient regions (holes) on the rigid polymer chains and electron-rich regions ($FeCl_4^-$ ions) between the polymer chains, thereby inducing charge carrier form. Consequently, the concentration of $FeCl_2$ species in the doped polymer blend film serves as an indicator of the number of charge carriers generated after doping. Hence, the doping efficiency (η_d) can be determined from the ratio of reduced dopant to the total dopant, as expressed by eq 2

$$\eta_d = \frac{A^-}{A^0 + A^-} \quad (2)$$

where A^0 is the area under the $FeCl_2$ peak, and A^- is the sum of the areas under the $FeCl_4^-$ peaks. Thus, the doping efficiencies of the doped **P3HT/SEBS** = 100/0 and 90/10 films are found to be approximately 64.6 and 78.2%, respectively, while those of the doped **PDVT-10/SEBS** = 100/0 and 90/10 films are 64.0 and 63.4%, respectively. Therefore, the doping efficiency of the polymer blend decreases in the following order: **P3HT/SEBS** = 90/10 > **P3HT/SEBS** = 100/0 > **PDVT-10/SEBS** = 100/0 > **PDVT-10/SEBS** = 90/10.

These results provide insights into the efficiency of the dopant reduction reaction in the polymer blend, which is related to the electrical conductivity. Generally, a higher doping efficiency may lead to an increased number density (n) of charge carriers. However, the relationship between doping efficiency and electrical conductivity is not always linear and can be influenced by factors such as the carrier mobility and the miscibility of $FeCl_3$ with the blend films. These aspects are explored in more detail in the following experiments.[48,52−55]

The relationship between the doping efficiency and the number density of charge carriers (or polarons) in **P3HT/SEBS** and **PDVT-10/SEBS** is elucidated by the Hall effect measurements in Figure 4d,e. Here, **P3HT/SEBS** = 90/10 (4.6×10^{20} cm^{-3}) exhibits a higher value than **P3HT/SEBS** = 100/0 (4.4×10^{20} cm^{-3}), followed by **PDVT-10/SEBS** = 100/0 (3.8×10^{20} cm^{-3}), and **PDVT-10/SEBS** = 90/10 (2.4×10^{20} cm^{-3}). This result is consistent with the higher concentration of $FeCl_4^-$ in the **P3HT/SEBS** = 90/10, as determined by the above-mentioned XPS analysis. Therefore, the observed trend in the number density of charge carriers aligns with that in the doping efficiency and supports the hypothesis that a higher doping efficiency leads to a higher number density of charge carriers in the polymer blend films.[52,55] The effects of miscibility on the various undoped polymer blend films are revealed by the contact angle measurements in Figure 4f, which indicate surface tensions of 11.1, 10.3, 11.4, and 12.7 mN m^{-1} for the $FeCl_3$ solution in contact with undoped **P3HT/SEBS** = 100/0, **P3HT/SEBS** = 90/10, **PDVT-10/SEBS** = 100/0, and **PDVT-10/SEBS** = 90/10, respectively. Remarkably, the pure $FeCl_3$ film is strongly wetted by water or glycerol droplets (Figure S7), thereby indicating an exceptionally low surface energy. Consequently, the surface tension discrepancies between $FeCl_3$ and the **P3HT/SEBS** blend films are relatively small compared to those of the **PDVT-10/SEBS** blend films, thus suggesting a decrease in the degree of miscibility with $FeCl_3$ in the following order: **P3HT/SEBS** = 90/10 > **P3HT/SEBS** = 100/0 > **PDVT-10/SEBS** = 100/0 > **PDVT-10/SEBS** = 90/10. These conclusions are further supported by the corresponding contact angle images in Figure S8, along with the contact angle and AFM measurements on the corresponding undoped polymer blend films in Figures S9 and S10. Thus, similar trends are observed in the root-mean-square roughness (R_{rms}) values of the doped **P3HT**-based and **PDVT-10/SEBS**-based films, with values of 2.50 and 4.02 nm, respectively, for the doped **P3HT/SEBS** = 90/10 films, **PDVT-10/SEBS** = 100/0 with R_{rms} = 5.27 nm, and **PDVT-10/SEBS** = 90/10 with R_{rms} = 8.17 nm. The lower R_{rms} values of the **P3HT/SEBS** films indicate better compatibility between $FeCl_3$ and these films, thereby suggesting a favorable interaction and relatively high doping efficiency. Taken together, these results demonstrate the influence of the dopant miscibility, wettability, and surface morphology of the polymer blend film on the doping efficiency, number density of charge carriers, and overall TE performance. However, despite the better compatibility between **P3HT/SEBS** and $FeCl_3$, doped **PDVT-10/SEBS** exhibits a higher electrical conductivity. This is primarily because the electrical conductivity is given by the product of the elementary charge (q), the Hall-effect mobility

https://doi.org/10.1021/acsami.3c15651
ACS Appl. Mater. Interfaces 2024, 16, 3764−3777

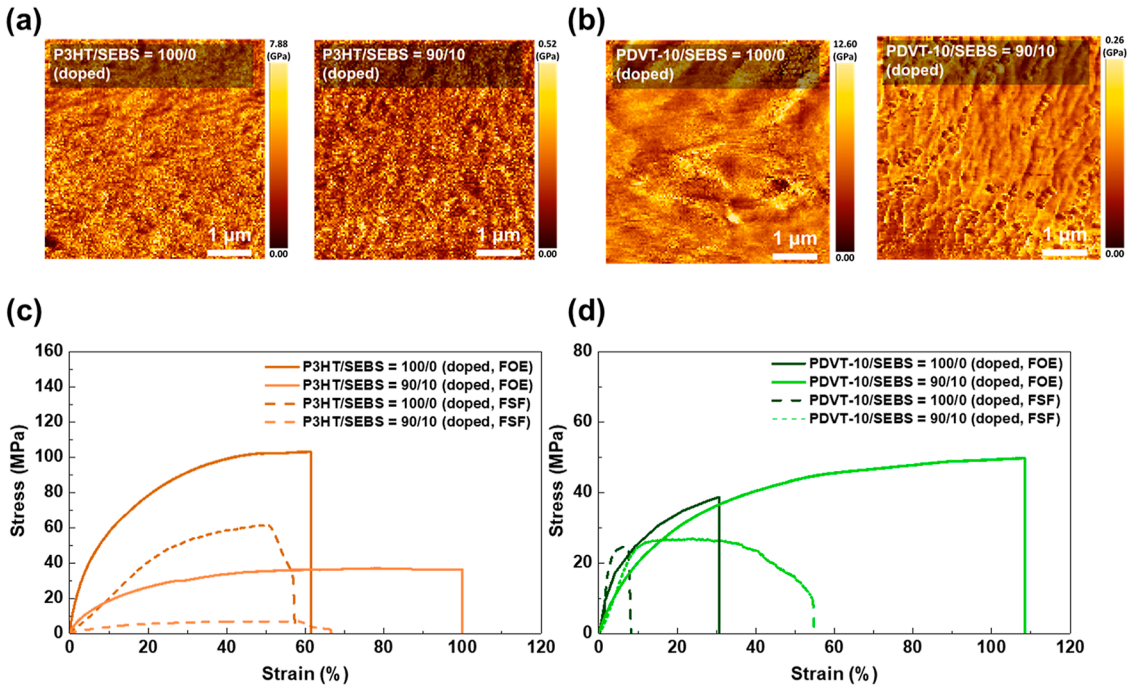

Figure 5. DMT Modulus mapping images obtained with AFM for doped (a) **P3HT/SEBS** = 100/0, 90/10 and (b) **PDVT-10/SEBS** = 100/0, 90/10 blend films. Tensile stress−strain curves for doped (c) **P3HT/SEBS** = 100/0, 90/10 and (d) **PDVT-10/SEBS** = 100/0, 90/10 blend films by FOE and FSF.

(μ_{Hall}), and the activation energy (E_A) of the doped film, as per eq 3

$$\sigma = qn\mu_{Hall} \tag{3}$$

Hence, the higher electrical conductivities of the doped **PDVT-10/SEBS** films result, in part, from their higher Hall-effect mobilities of 4.6 and 3.0 $cm^2\ V^{-1}\ s^{-1}$ compared to 1.8 and 1.9 $cm^2\ V^{-1}\ s^{-1}$ for the doped **P3HT/SEBS** films (Figure 4a−c,e).[48,56]

Meanwhile, the activation energy (E_A) reflects the presence of transport barriers in the doped **P3HT/SEBS** and **PDVT-10/SEBS** films, which can be determined by fitting the temperature-dependent electrical conductivities in Figure 4g to the Arrhenius model. Here, the electrical conductivity of each film is seen to decrease as the temperature decreases from 322 to 285 K, which is consistent with thermally activated transport in an organic semiconductor. The calculated activation energies are 125.68 and 183.72 meV for the doped 100/0 **PDVT-10/SEBS** = 100/0 and 90/10, respectively, compared to 229.31 and 192.11 meV, respectively, for the doped **P3HT/SEBS** = 100/0 and 90/10. The lower activation energies of the **PDVT-10/SEBS** films indicate a lower energy barrier for charge transport, which further contributes to the higher electrical conductivity. In turn, the lower activation energies of these films can be attributed to their edge-on molecular orientations, as observed in Figure 2 above, which may enhance the Hall mobility, thereby resulting in a higher electrical conductivity, despite the relatively low compatibility with $FeCl_3$. By contrast, the bimodal orientations of the **P3HT/SEBS** films may not only enhance the miscibility with $FeCl_3$ but also result in a lower Hall mobility and a higher activation energy than those of the **PDVT-10/SEBS** films.[57]

Although the observed trends in the electrical conductivities are well explained by the above considerations, the increase in the Seebeck coefficient of the doped **P3HT/SEBS** = 90/10 film compared to the doped **P3HT/SEBS** = 100/0 film, and the decrease in the Seebeck coefficient of the doped **PDVT-10/SEBS** = 90/10 film relative to the doped **PDVT-10/SEBS** = 100/0 film, remain to be explained. The Seebeck coefficient (S) is a crucial parameter that characterizes the material's ability to generate a voltage difference in response to a temperature gradient. It is influenced by the energy levels and transport properties of the charge carriers within the material, and can be calculated using eq 4

$$S = \frac{k_B}{q}\left(\frac{E_F - E_V}{k_B T}\right) \tag{4}$$

where E_F and E_V are the energy levels of the Fermi level and valence band, respectively, k_B is Boltzmann's constant, and T is the absolute temperature. Thus, the Seebeck coefficient is directly related to the difference between E_F and E_V, (i.e., $E_F - E_V$), which can be determined from the energy levels measured by ultraviolet−visible (UV−vis) and ultraviolet photoelectron spectroscopy (UPS), as shown in Figures S12 and S13. According to Figure S13, the $E_F - E_V$ value of **P3HT/SEBS** = 100/0 is 0.52 eV, which is much higher than the value of 0.20 eV of **PDVT-10/SEBS** = 100/0. Therefore, the Seebeck coefficient of **P3HT/SEBS** = 100/0 is far better than the Seebeck coefficient of **PDVT-10/SEBS**. Besides, the $E_F - E_V$ values exhibited variations of 0.52, 0.55, 0.20, and 0.18 eV, which are comparable to the S values observed for doped **P3HT/SEBS** = 100/0, 90/10 and **PDVT-10/SEBS** = 100/0, 90/10, respectively. The trend in the S values is as follows: **P3HT/SEBS** = 90/10 > **P3HT/SEBS** = 100/0 > **PDVT-10/SEBS** = 100/0 > **PDVT-10/SEBS** = 90/10.[58,59]

Taken together, the above results indicate that the electrical conductivities of the doped polymer blend films are influenced by the doping efficiency, the Hall mobility, and the activation energy, while the TE properties (particularly the Seebeck

https://doi.org/10.1021/acsami.3c15651
ACS Appl. Mater. Interfaces 2024, 16, 3764−3777

Table 1. Mechanical Parameters for Doped P3HT/SEBS = 100/0, 90/10 and PDVT-10/SEBS = 100/0, 90/10 Blend Films by FOE and FSF

sample name	film on elastomer			free standing film			DMT modulus [GPa]
	COS [%]	*E* [MPa]	UTS [MPa]	COS [%]	*E* [MPa]	UTS [MPa]	
doped **P3HT/SEBS** = 100/0	61.7	1450.4	103.2	57.4	898.0	61.3	3.8
doped **P3HT/SEBS** = 90/10	100.0	326.7	36.2	66.7	300.2	6.9	0.3
doped **PDVT-10/SEBS** = 100/0	30.8	281.0	24.5	8.4	918.8	15.2	7.4
doped **PDVT-10/SEBS** = 90/10	108.1	262.6	49.6	54.8	165.1	26.3	0.1

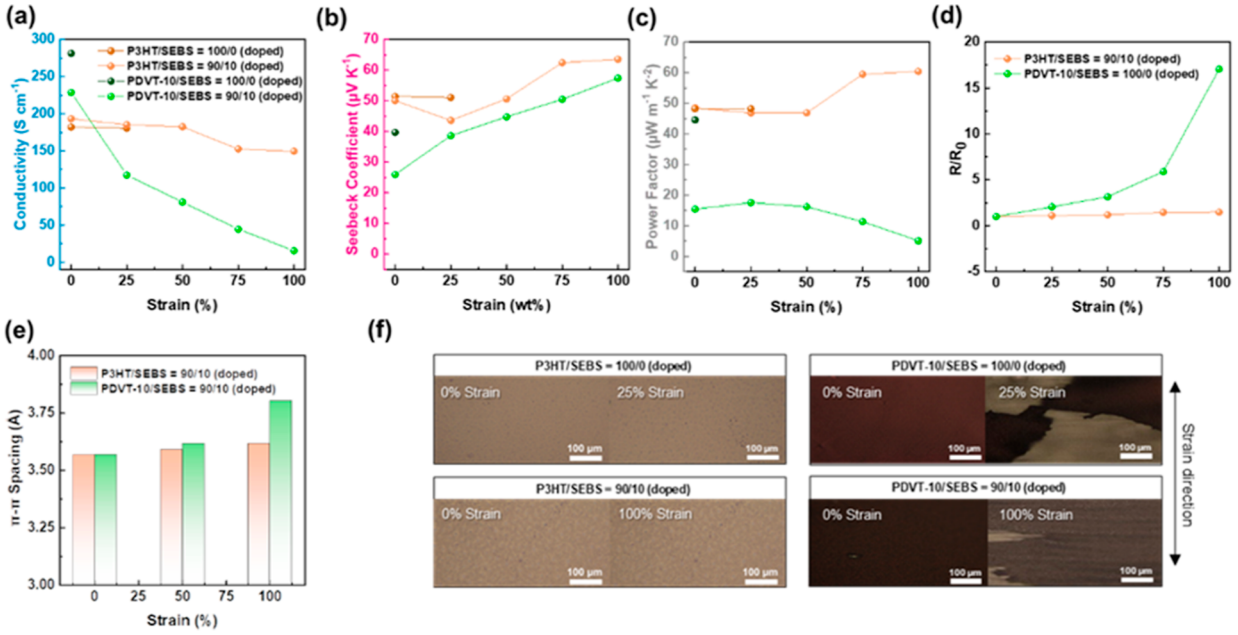

Figure 6. (a) σ, (b) *S*, (c) *PF*, and (d) R/R_0 for doped **P3HT/SEBS** = 100/0, 90/10, and **PDVT-10/SEBS** = 100/0, 90/10 blend films under various tensile strains. (e) Change in $d_{(010)}$ of doped **P3HT/SEBS** = 90/10, and **PDVT-10/SEBS** = 90/10 blend films under various tensile strains. (f) OM images for doped **P3HT/SEBS** = 100/0, 90/10, and **PDVT-10/SEBS** = 100/0, 90/10 blend films under various tensile strains.

coefficients) are influenced by the energy level differences. Hence, by understanding and optimizing these factors, the electrical conductivities and TE performances of the **P3HT/SEBS** and **PDVT-10/SEBS** blend films may be enhanced simultaneously.

Mechanical and Thermoelectric Properties of the Doped Polymer Blend Films under Stretching. The mechanical properties of doped **P3HT/SEBS** = 100/0, 90/10 and **PDVT-10/SEBS** = 100/0, 90/10 blends were characterized, including the determination of ultimate tensile strength (UTS) and analysis using the Derjaguin-Muller-Toporov (DMT) contact mechanics model (Figure 5 and Table 1). Thus, the elastic moduli of the doped **P3HT/SEBS** = 100/0, 90/10 and **PDVT-10/SEBS** = 100/0, 90/10 blends are 3.8, 0.2, 7.4, and 0.2 GPa, respectively (Figures 5a,b and S11). Notably, the addition of 10 wt % **SEBS** significantly enhances the deformability and stretchability of each polymer blend. This can be attributed to the introduction of the flexible elastic polymer component, which forms entangled amorphous **SEBS** domains within each film. These domains can dissipate the strain energy and protect the rigid polymer component from damage during stretching. Tensile testing was performed using the film-on-elastomer (FOE) and free-standing-film (FSF) methods to evaluate the comprehensive mechanical properties of doped blend films. In the FOE method, the doped blend films on the ODTS-treated glass substrates were carefully transferred onto 3M VHB tape, while the FSF method involved gentle peeling off of the films from the ODTS-treated glass substrate. These techniques allowed for the characterization of the films' mechanical response under tensile loading conditions. Furthermore, Figure 5c,d indicates that the crack-onset strain (COS) values of the doped **P3HT/SEBS** = 100/0, 90/10 and **PDVT-10/SEBS** = 100/0, 90/10 blends are 61.7, 100.0, 30.8, and 108.1%, respectively, in the film on FOE configuration and 57.4, 66.7, 8.4, and 54.8%, respectively, in the FSF configuration. Importantly, both rigid polymer blends display COS values exceeding 100.0%, thereby indicating a significant increase in stretchability.

As indicated in Table 1, the **P3HT/SEBS** = 90/10 and **PDVT-10/SEBS** = 90/10 films exhibit significantly lower elastic moduli (*E* = 300.2 and 165.1, respectively) compared to those of the purely rigid polymer films (*E* = 898.0 and 918.8, respectively). Moreover, the elastic moduli of the blends are similar to those of the human skin and common elastomers, thereby suggesting potential applications in wearable electronics.[3] Furthermore, the doped **P3HT/SEBS** = 100/0 films exhibit large deformations before breaking, thus resulting in high UTS values of 103.2 and 61.3 MPa in the FOE and FSF configurations, respectively. Thus, the addition of 10 wt % **SEBS** increases the deformation of the doped **P3HT** film and results in higher COS values for both types of rigid polymer films. However, the doped **PDVT-10/SEBS** = 100/0, 90/10 blend films each exhibit similar UTS values in the range of tens of MPa. This can be attributed to the stronger interconnec-

https://doi.org/10.1021/acsami.3c15651
ACS Appl. Mater. Interfaces 2024, 16, 3764−3777

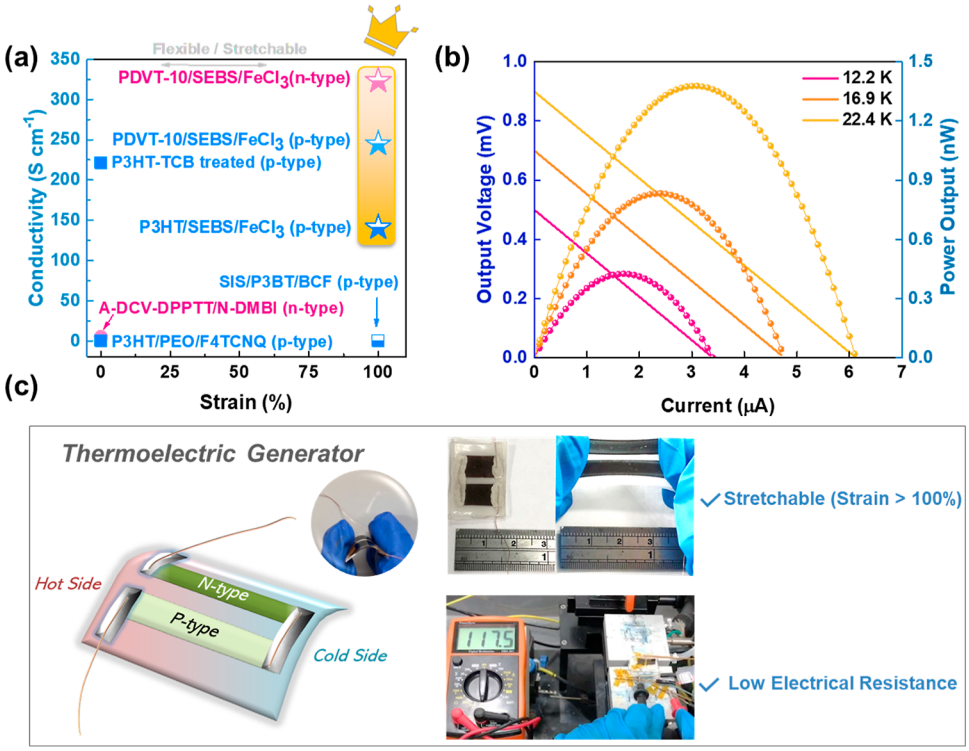

Figure 7. (a) Measured σ of fully flexible/stretchable doped organic semiconducting TE devices under tensile strain. (b) Performance characterization of output characteristic of P−N integrated TEG under various ΔT of 12.2, 16.9, and 22.4 K. (c) Schematic representation of the configuration of a p−n integrated TEG, showcasing its excellent stretchability and low resistance conditions.

tions between the rigid **PDVT-10** domains, which play a dominant role in determining the UTS in both the presence and absence of **SEBS**. The interconnected **PDVT-10** domains may also contribute to the higher conductivity of the **PDVT-10/SEBS** blends.[60−62]

The results in Figure 6 reveal the influence of tensile stretching on the TE properties of the polymer blend films in the FOE configuration. Here, the doped **P3HT/SEBS** = 100/0 film exhibits slight variations in electrical conductivity (Figure 6a), Seebeck coefficient (Figure 6b), and power factor (Figure 6c), but eventually cracks at a strain of 25%. By contrast, doped **PDVT-10/SEBS** = 100/0 does not exhibit any stretchability and fails to withstand the applied strain of even 25%. However, with the addition of 10 wt % **SEBS**, both the doped **P3HT/SEBS** = 90/10 and **PDVT-10/SEBS** = 90/10 blends show the ability to stretch up to 100% tensile strain. Under stretching, these two blends each exhibit a decrease in electrical conductivity and an increase in the Seebeck coefficient. However, these variations are notably smaller for doped **P3HT/SEBS** = 90/10 than for doped **PDVT-10/SEBS** = 90/10. Furthermore, the variations in the relative resistance (R/R_0) is shown in Figure 6d, where the doped **P3HT/SEBS** = 90/10 exhibits a more stable behavior than that of the **PDVT-10/SEBS** = 90/10 within the strain range of 0−100%. The considerable increase in R/R_0 for doped **PDVT-10/SEBS** = 90/10 during stretching can be attributed to the presence of cracks in the film, as observed in the OM image in Figure 6f. Furthermore, the GIWAXS analyses in Figure 6e reveal that the doped **PDVT-10/SEBS** = 90/10 blend has a significantly higher $d_{(010)}$ value than that of doped **P3HT/SEBS** = 90/10, thereby indicating a higher occurrence of defects that can disrupt the charge carrier transport pathway.

Stretchable p−n Junction TEG Based on the Doped Semiconducting Polymer Blend. To realize the p−n junction in the stretchable TE device, p- and n-type TE films were fabricated using the **PDVT-10/SEBS** = 90/10 polymer blend with $FeCl_3$ concentrations of 5 and 81 mg mL^{-1}. In each case, the film was immersed in the doping solution for 5 min to ensure effective doping. Because this doping process follows the polarity switching mechanism proposed by Wang et al., the **PDVT-10/SEBS** = 90/10 film experiences a transition from p-type to n-type at an $FeCl_3$ concentration of 81 mg mL^{-1}.[44,63] In accordance with eq 4, the energy levels, as determined through UV−vis spectroscopy and UPS as illustrated in Figure S14, signify a discernible shift in polarity within the donor−acceptor polymer films. This shift, transitioning from the p-type to n-type, is ascribed to the intersection of the Fermi level with the HOMO of the donor−acceptor copolymer, particularly notable at increased concentrations of $FeCl_3$. Moreover, the n-type device exhibits remarkable TE properties, including a high electrical conductivity of 323.2 S cm^{-1}, a Seebeck coefficient of −15.7 μV K^{-1}, and a notable power factor of 7.9 μW m^{-1} K^{-2}.

As noted above, achieving high electrical conductivity while retaining the flexibility/stretchability of the doped organic semiconducting TE device presents a significant challenge. This challenge stems from the intricate interplay between microstructural crystallinity and the planarity of conjugated polymer backbones, which jointly influence the electrical conductivity and flexibility of the thin films. The electrical conductivities of the as-fabricated and previously reported fully flexible/stretchable doped TE devices under various tensile strains are compared in Figure 7a, and the details are provided in Table S3. Importantly, the as-fabricated p-doped **P3HT/SEBS** = 90/10 and n- or p-doped **PDVT-10/SEBS** = 90/10

https://doi.org/10.1021/acsami.3c15651
ACS Appl. Mater. Interfaces 2024, 16, 3764−3777

films exhibit electrical conductivities approximately 2 orders of magnitude higher than the maximum electrical conductivity observed among the previously reported TE devices.[15,16,21,64]

Finally, a stretchable doped semiconducting polymer-blend p−n junction TEG device was successfully fabricated by integrating the p-type and n-type films, as shown schematically in Figure 7c and Movie S1. In detail, the **PDVT-10**/**SEBS** = 90/10 solution was first drop cast onto an ODTS-treated glass substrate, as shown in Figure 1. The p-type and n-type doping processes were then performed by immersing the polymer blend films in a 5 mg mL^{-1} $FeCl_3$/acetonitrile solution for 5 min and an 81 mg mL^{-1} $FeCl_3$/acetonitrile solution for 5 min, respectively. The p- and n-doped films were then transferred onto separate sections of 3M VHB tape and connected by using copper wires and silver conducting pastes. To ensure stability, the TEG device was carefully encapsulated by applying tape on the top side within a nitrogen-filled glovebox. The output characteristics of the flexible integrated p−n **PDVT-10**/**SEBS** TEGs under various temperature gradients (ΔT) of 12.2, 16.9, and 22.4 K are presented in Figure 7b. Here, the maximum current and output power are 6.08 μA and 1.39 nW, respectively, as ΔT is increased from 12.2 to 22.4 K. The measured output voltage (ΔV) can be compared with the theoretical value obtained from eq 5

$$\Delta V = (S_p + |S_n|)\Delta T \quad (5)$$

As shown in Figure 4b and Table S3, the Seebeck coefficient of the p-type leg (S_p) is approximately 26.0 μV K^{-1}, while that of the n-type leg (S_n) is approximately −15.7 μV K^{-1}. Thus, at a ΔT of 22.4 K, the calculated output voltage is 0.94 mV, which aligns closely with the above-mentioned experimental value. The mechanical stretchability of the as-fabricated **PDVT-10**/**SEBS** = 90/10 p−n junction TEG is further demonstrated in Figure 7c.[15,16,21,65] In brief, a stretchable doped semiconducting polymer blend-based TEG was successfully fabricated herein by integrating p- and n-type devices. The TEG exhibited an impressive mechanical stretchability, capable of withstanding tensile strains of up to 100%, along with excellent ambient stability and a low electrical resistance due to the encapsulation process. These findings highlight the potential of doped semiconducting polymer blend-based TEG devices for flexible/stretchable energy harvesting applications.

CONCLUSIONS

Herein, a comprehensive investigation was presented on the effects of blending a rigid polymer and an elastic polymer on the thermoelectric (TE) properties of a stretchable doped semiconducting material. For comparison, either the donor polymer poly(3-hexylthiophene) (**P3HT**) or the donor−acceptor polymer poly(3,6-dithiophen-2-yl-2,5-di(2-decyltetradecyl)-pyrrolo[3,4-*c*]pyrrole-1,4-dione-alt-thienylenevinylene-2,5-yl) (**PDVT-10**) was blended with styrene-ethylene-butylene-styrene (**SEBS**). The effects of various blend ratios of rigid polymer to **SEBS** on the morphologies, mechanical properties, and TE performances were examined. The results indicated that a relatively low **SEBS** composition of 10 wt % leads to preferential doping along the long-range crystallite regions of the continuous network morphology, thereby resulting in an expansion of the lamellar spacing ($d_{(100)}$) and a decrease in the π−π spacing ($d_{(010)}$). This enhances the mechanical properties, while maintaining the TE properties, with only minimal variation compared to those of the doped rigid polymers in the absence of **SEBS**. The most favorable combinations of TE and tensile strain properties were obtained at an optimal blend ratio of 10 wt % **SEBS** with each flexible polymer. Meanwhile, the doped **P3HT** blend with a **P3HT**/**SEBS** ratio of 90/10 demonstrates a slightly better TE performance than that of the doped **P3HT** in the absence of **SEBS**. In detail, the doped blend exhibits an electrical conductivity, Seebeck coefficient, and power factor of 140.9 S cm^{-1}, 60.6 μV K^{-1}, and 51.8 μW m^{-1} K^{-1}, respectively, compared to the doped single polymer. These results suggest that the polymer blend has minimal impact on the crystallinity and molecular alignment in the doped **P3HT**/**SEBS** = 90/10, indicating a higher doping efficiency and number density of charge carriers along with better miscibility of the polymer with the doping solution. By contrast, the doped **PDVT-10**/**SEBS** = 90/10 exhibits a slightly poorer TE performance than the doped **PDVT-10**, with the former exhibiting an electrical conductivity, Seebeck coefficient, and power factor of 244.9 S cm^{-1}, 37.6 μV K^{-1}, and 34.6 μW m^{-1} K^{-1}, respectively. This is because the incorporation of **SEBS** disrupts the edge-on alignment of **PDVT-10**, thereby inhibiting the charge-carrier transport pathway.

In addition, the mechanical and TE properties of the blends were examined under various stretching conditions. The results indicated that the TE properties of the doped **P3HT**/**SEBS** = 90/10 are more stable within the 0−100% strain range compared to those of the doped **PDVT-10**/**SEBS** = 90/10. This is attributed to the disturbance of the preferred edge-on charge-carrier transport pathway in doped **PDVT-10**/**SEBS** = 90/10 during stretching.

Finally, a stretchable doped semiconducting polymer blend-based p−n junction TEG was successfully fabricated and shown to possess remarkable mechanical stretchability with the ability to withstand tensile strains of up to 100%. Moreover, the TEG device maintained a low electrical resistance of 117.5 Ω due to the encapsulation process. These significant achievements emphasize the vast potential of the stretchable doped semiconducting polymer blend-based TEGs for applications requiring flexibility/stretchability in energy harvesting.

ASSOCIATED CONTENT

Supporting Information

The Supporting Information is available free of charge at https://pubs.acs.org/doi/10.1021/acsami.3c15651.

Materials, instrumentation, optical images, AFM phase images, SEM images, UV−vis−NIR absorbance spectra, 2D-GIWAXS images, AFM-derived DMT modulus mapping histogram images, UPS secondary electron cutoff (SECO) and HOMO onset energies, and energy level diagrams (PDF)

Low resistance condition of a p−n integrated TEG (MP4)

AUTHOR INFORMATION

Corresponding Author

Cheng-Liang Liu − *Department of Materials Science and Engineering, National Taiwan University, Taipei 10617, Taiwan;* orcid.org/0000-0002-8778-5386; Email: liucl@ntu.edu.tw

https://doi.org/10.1021/acsami.3c15651
ACS Appl. Mater. Interfaces 2024, 16, 3764−3777

Authors

Yun Chang − *Department of Materials Science and Engineering, National Taiwan University, Taipei 10617, Taiwan*

Yi-Hsuan Huang − *Department of Materials Science and Engineering, National Taiwan University, Taipei 10617, Taiwan*

Po-Shen Lin − *Department of Materials Science and Engineering, National Taiwan University, Taipei 10617, Taiwan*

Shao-Huan Hong − *Department of Materials Science and Engineering, National Taiwan University, Taipei 10617, Taiwan*

Shih-Huang Tung − *Institute of Polymer Science and Engineering, National Taiwan University, Taipei 10617, Taiwan;* orcid.org/0000-0002-6787-4955

Complete contact information is available at: https://pubs.acs.org/10.1021/acsami.3c15651

Author Contributions

[§]Y.C. authors contributed equally to this work.

Notes

The authors declare no competing financial interest.

■ ACKNOWLEDGMENTS

C.-L.L. acknowledges the financial support from 2030 Cross-Generation Young Scholars Program by the National Science and Technology Council (NSTC) in Taiwan under grant 111-2628-E-002-014 and 112-2628-E-002-013, Academic Research-Career Development Project (Sprout Research Projects) by National Taiwan University (NTU112L7856), and Advanced Research Center for Green Materials Science and Technology from The Featured Area Research Center Program within the framework of the Higher Education Sprout Project by the Ministry of Education (112L9006). The authors thank Beamline TLS 13A at National Synchrotron Radiation Research Center (NSRRC) of Taiwan for providing beamtime.

■ REFERENCES

(1) Fan, W.; An, Z.; Liu, F.; Gao, Z.; Zhang, M.; Fu, C.; Zhu, T.; Liu, Q.; Zhao, X. High-Performance Stretchable Thermoelectric Generator for Self-Powered Wearable Electronics. *Adv. Sci.* **2023**, *10*, 2206397.

(2) Deng, L.; Liu, Y.; Zhang, Y.; Wang, S.; Gao, P. Organic Thermoelectric Materials: Niche Harvester of Thermal Energy. *Adv. Funct. Mater.* **2023**, *33*, 2210770.

(3) Jia, Y.; Jiang, Q.; Sun, H.; Liu, P.; Hu, D.; Pei, Y.; Liu, W.; Crispin, X.; Fabiano, S.; Ma, Y.; Cao, Y. Wearable Thermoelectric Materials and Devices for Self-Powered Electronic Systems. *Adv. Mater.* **2021**, *33*, 2102990.

(4) Massetti, M.; Jiao, F.; Ferguson, A. J.; Zhao, D.; Wijeratne, K.; Würger, A.; Blackburn, J. L.; Crispin, X.; Fabiano, S. Unconventional Thermoelectric Materials for Energy Harvesting and Sensing Applications. *Chem. Rev.* **2021**, *121*, 12465−12547.

(5) Zhao, W.; Ding, J.; Zou, Y.; Di, C.-a.; Zhu, D. Chemical doping of organic semiconductors for thermoelectric applications. *Chem. Soc. Rev.* **2020**, *49*, 7210−7228.

(6) DiSalvo, F. J. Thermoelectric Cooling and Power Generation. *Science* **1999**, *285*, 703−706.

(7) Pataki, N.; Rossi, P.; Caironi, M. Solution processed organic thermoelectric generators as energy harvesters for the Internet of Things. *Appl. Phys. Lett.* **2022**, *121*, 230501.

(8) Hasan, M. N.; Nafea, M.; Nayan, N.; Mohamed Ali, M. S. Thermoelectric Generator: Materials and Applications in Wearable Health Monitoring Sensors and Internet of Things Devices. *Adv. Mater. Technol.* **2022**, *7*, 2101203.

(9) Liu, Y.; Wang, X.; Hou, S.; Wu, Z.; Wang, J.; Mao, J.; Zhang, Q.; Liu, Z.; Cao, F. Scalable-produced 3D elastic thermoelectric network for body heat harvesting. *Nat. Commun.* **2023**, *14*, 3058.

(10) Zhang, D.; Wang, Y.; Yang, Y. Design, Performance, and Application of Thermoelectric Nanogenerators. *Small* **2019**, *15*, 1805241.

(11) Xia, J.; Liang, C.; Gu, H.; Mei, S.; Li, S.; Zhang, N.; Chen, S.; Cai, Y.; Xing, G. Surface Passivation Toward Efficient and Stable Perovskite Solar Cells. *Energy Environ. Mater.* **2023**, *6*, No. e12296.

(12) Cao, T.; Shi, X.-L.; Chen, Z.-G. Advances in the design and assembly of flexible thermoelectric device. *Prog. Mater. Sci.* **2023**, *131*, 101003.

(13) He, H.; Ouyang, J. Enhancements in the Mechanical Stretchability and Thermoelectric Properties of PEDOT:PSS for Flexible Electronics Applications. *Acc. Mater. Res.* **2020**, *1*, 146−157.

(14) Zhang, L.; Shi, X.-L.; Yang, Y.-L.; Chen, Z.-G. Flexible thermoelectric materials and devices: From materials to applications. *Mater. Today* **2021**, *46*, 62−108.

(15) Kiefer, D.; Yu, L.; Fransson, E.; Gómez, A.; Primetzhofer, D.; Amassian, A.; Campoy-Quiles, M.; Müller, C. A Solution-Doped Polymer Semiconductor:Insulator Blend for Thermoelectrics. *Adv. Sci.* **2017**, *4*, 1600203.

(16) Jeong, Y. J.; Jung, J.; Suh, E. H.; Yun, D.-J.; Oh, J. G.; Jang, J. Self-Healable and Stretchable Organic Thermoelectric Materials: Electrically Percolated Polymer Nanowires Embedded in Thermoplastic Elastomer Matrix. *Adv. Funct. Mater.* **2020**, *30*, 1905809.

(17) Xu, J.; Wu, H.-C.; Zhu, C.; Ehrlich, A.; Shaw, L.; Nikolka, M.; Wang, S.; Molina-Lopez, F.; Gu, X.; Luo, S.; Zhou, D.; Kim, Y.-H.; Wang, G.-J. N.; Gu, K.; Feig, V. R.; Chen, S.; Kim, Y.; Katsumata, T.; Zheng, Y.-Q.; Yan, H.; Chung, J. W.; Lopez, J.; Murmann, B.; Bao, Z. Multi-scale ordering in highly stretchable polymer semiconducting films. *Nat. Mater.* **2019**, *18*, 594−601.

(18) Xu, J.; Wang, S.; Wang, G.-J. N.; Zhu, C.; Luo, S.; Jin, L.; Gu, X.; Chen, S.; Feig, V. R.; To, J. W. F.; Rondeau-Gagné, S.; Park, J.; Schroeder, B. C.; Lu, C.; Oh, J. Y.; Wang, Y.; Kim, Y.-H.; Yan, H.; Sinclair, R.; Zhou, D.; Xue, G.; Murmann, B.; Linder, C.; Cai, W.; Tok, J. B. H.; Chung, J. W.; Bao, Z. Highly stretchable polymer semiconductor films through the nanoconfinement effect. *Science* **2017**, *355*, 59−64.

(19) Gregory, S. A.; Menon, A. K.; Ye, S.; Seferos, D. S.; Reynolds, J. R.; Yee, S. K. Effect of Heteroatom and Doping on the Thermoelectric Properties of Poly(3-alkylchalcogenophenes). *Adv. Energy Mater.* **2018**, *8*, 1802419.

(20) Yee, P. Y.; Scholes, D. T.; Schwartz, B. J.; Tolbert, S. H. Dopant-Induced Ordering of Amorphous Regions in Regiorandom P3HT. *J. Phys. Chem. Lett.* **2019**, *10*, 4929−4934.

(21) Qu, S.; Yao, Q.; Wang, L.; Chen, Z.; Xu, K.; Zeng, H.; Shi, W.; Zhang, T.; Uher, C.; Chen, L. Highly anisotropic P3HT films with enhanced thermoelectric performance via organic small molecule epitaxy. *NPG Asia Mater.* **2016**, *8*, No. e292.

(22) Wu, L.; Li, H.; Chai, H.; Xu, Q.; Chen, Y.; Chen, L. Anion-Dependent Molecular Doping and Charge Transport in Ferric Salt-Doped P3HT for Thermoelectric Application. *ACS Appl. Electron. Mater.* **2021**, *3*, 1252−1259.

(23) Thomas, E. M.; Davidson, E. C.; Katsumata, R.; Segalman, R. A.; Chabinyc, M. L. Branched Side Chains Govern Counterion Position and Doping Mechanism in Conjugated Polythiophenes. *ACS Macro Lett.* **2018**, *7*, 1492−1497.

(24) Zhong, Y.; Untilova, V.; Muller, D.; Guchait, S.; Kiefer, C.; Herrmann, L.; Zimmermann, N.; Brosset, M.; Heiser, T.; Brinkmann, M. Preferential Location of Dopants in the Amorphous Phase of Oriented Regioregular Poly(3-hexylthiophene-2,5-diyl) Films Helps Reach Charge Conductivities of 3000 S cm-1. *Adv. Funct. Mater.* **2022**, *32*, 2202075.

(25) Hong, C. T.; Yoo, Y.; Kang, Y. H.; Ryu, J.; Cho, S. Y.; Jang, K.-S. Effect of film thickness and crystallinity on the thermoelectric properties of doped P3HT films. *RSC Adv.* **2015**, *5*, 11385−11391.
(26) Tang, J.; Ji, J.; Chen, R.; Yan, Y.; Zhao, Y.; Liang, Z. Achieving Efficient p-Type Organic Thermoelectrics by Modulation of Acceptor Unit in Photovoltaic π-Conjugated Copolymers. *Adv. Sci.* **2022**, *9*, 2103646.
(27) Wang, S.; Zuo, G.; Kim, J.; Sirringhaus, H. Progress of Conjugated Polymers as Emerging Thermoelectric Materials. *Prog. Polym. Sci.* **2022**, *129*, 101548.
(28) Liao, Z.; Zhou, X.; Wei, G.; Wang, S.; Gao, C.; Wang, L. Intrinsically Self-Healable and Wearable All-Organic Thermoelectric Composite with High Electrical Conductivity for Heat Harvesting. *ACS Appl. Mater. Interfaces* **2022**, *14*, 43421−43430.
(29) Tripathi, A.; Lee, Y.; Lee, S.; Woo, H. Y. Recent advances in n-type organic thermoelectric materials, dopants, and doping strategies. *J. Mater. Chem. C* **2022**, *10*, 6114−6140.
(30) Zhang, Y.; Wang, W.; Zhang, F.; Dai, K.; Li, C.; Fan, Y.; Chen, G.; Zheng, Q. Soft Organic Thermoelectric Materials: Principles, Current State of the Art and Applications. *Small* **2022**, *18*, 2104922.
(31) Xu, S.; Shi, X.-L.; Dargusch, M.; Di, C.; Zou, J.; Chen, Z.-G. Conducting polymer-based flexible thermoelectric materials and devices: From mechanisms to applications. *Prog. Mater. Sci.* **2021**, *121*, 100840.
(32) Emerson, J. A.; Toolan, D. T. W.; Howse, J. R.; Furst, E. M.; Epps, T. H., III Determination of Solvent-Polymer and Polymer-Polymer Flory-Huggins Interaction Parameters for Poly(3-hexylthiophene) via Solvent Vapor Swelling. *Macromolecules* **2013**, *46*, 6533−6540.
(33) Kim, J. Y.; Noh, S.; Nam, Y. M.; Kim, J. Y.; Roh, J.; Park, M.; Amsden, J. J.; Yoon, D. Y.; Lee, C.; Jo, W. H. Effect of Nanoscale SubPc Interfacial Layer on the Performance of Inverted Polymer Solar Cells Based on P3HT/PC71BM. *ACS Appl. Mater. Interfaces* **2011**, *3*, 4279−4285.
(34) Jeon, K.-H.; Park, J.-W. Light-Emitting Polymer Blended with Elastomers for Stretchable Polymer Light-Emitting Diodes. *Macromolecules* **2022**, *55*, 8311−8320.
(35) Yau, M. Y. E.; Gunkel, I.; Hartmann-Azanza, B.; Akram, W.; Wang, Y.; Thurn-Albrecht, T.; Steinhart, M. Semicrystalline Block Copolymers in Rigid Confining Nanopores. *Macromolecules* **2017**, *50*, 8637−8646.
(36) Park, B.; Kang, H.; Ha, Y. H.; Kim, J.; Lee, J.-H.; Yu, K.; Kwon, S.; Jang, S.-Y.; Kim, S.; Jeong, S.; Hong, S.; Byun, S.; Kwon, S.-K.; Kim, Y.-H.; Lee, K. Direct Observation of Confinement Effects of Semiconducting Polymers in Polymer Blend Electronic Systems. *Adv. Sci.* **2021**, *8*, 2100332.
(37) Ding, Y.; Zhu, Y.; Wang, H.; Wang, Y.; Gu, X.; Wang, X.; Qiu, L. Improving Electrical and Mechanical Properties of Blend Films via Optimizing Solution-Processable Techniques and Controlling the Semiconductor Molecular Weight. *Macromolecules* **2022**, *55*, 8577−8589.
(38) Wang, X.; Lee, W. H.; Zhang, G.; Wang, X.; Kang, B.; Lu, H.; Qiu, L.; Cho, K. Self-stratified semiconductor/dielectric polymer blends: vertical phase separation for facile fabrication of organic transistors. *J. Mater. Chem. C* **2013**, *1*, 3989−3998.
(39) Walheim, S.; Böltau, M.; Mlynek, J.; Krausch, G.; Steiner, U. Structure Formation via Polymer Demixing in Spin-Cast Films. *Macromolecules* **1997**, *30*, 4995−5003.
(40) Saitta, A. M.; Datchi, F. Structure and phase diagram of high-density water: The role of interstitial molecules. *Phys. Rev. E* **2003**, *67*, 020201.
(41) Newby, B.-m. Z.; Composto, R. J. Influence of Lateral Confinement on Phase Separation in Thin Film Polymer Blends. *Macromolecules* **2000**, *33*, 3274−3282.
(42) Zheng, Y.; Zhang, S.; Tok, J. B. H.; Bao, Z. Molecular Design of Stretchable Polymer Semiconductors: Current Progress and Future Directions. *J. Am. Chem. Soc.* **2022**, *144*, 4699−4715.
(43) Lei, Y.; Deng, P.; Li, J.; Lin, M.; Zhu, F.; Ng, T.-W.; Lee, C.-S.; Ong, B. S. Solution-Processed Donor-Acceptor Polymer Nanowire Network Semiconductors For High-Performance Field-Effect Transistors. *Sci. Rep.* **2016**, *6*, 24476.
(44) Wang, J.; Wang, Y.; Li, Q.; Li, Z.; Li, K.; Wang, H. P-Type Chemical Doping-Induced High Bipolar Electrical Conductivities in a Thermoelectric Donor-Acceptor Copolymer. *CCS Chem.* **2021**, *3*, 2482−2493.
(45) Khim, D.; Luzio, A.; Bonacchini, G. E.; Pace, G.; Lee, M.-J.; Noh, Y.-Y.; Caironi, M. Uniaxial Alignment of Conjugated Polymer Films for High-Performance Organic Field-Effect Transistors. *Adv. Mater.* **2018**, *30*, 1705463.
(46) Lee, B. H.; Hsu, B. B. Y.; Patel, S. N.; Labram, J.; Luo, C.; Bazan, G. C.; Heeger, A. J. Flexible Organic Transistors with Controlled Nanomorphology. *Nano Lett.* **2016**, *16*, 314−319.
(47) Luo, C.; Kyaw, A. K. K.; Perez, L. A.; Patel, S.; Wang, M.; Grimm, B.; Bazan, G. C.; Kramer, E. J.; Heeger, A. J. General Strategy for Self-Assembly of Highly Oriented Nanocrystalline Semiconducting Polymers with High Mobility. *Nano Lett.* **2014**, *14*, 2764−2771.
(48) Tsai, C.-H.; Lin, Y.-C.; Wu, W.-N.; Tung, S.-H.; Chen, W.-C.; Liu, C.-L. Optimizing the doping efficiency and thermoelectric properties of isoindigo-based conjugated polymers using side chain engineering. *J. Mater. Chem. C* **2023**, *11*, 6874−6883.
(49) Liang, Z.; Zhang, Y.; Souri, M.; Luo, X.; Boehm, A. M.; Li, R.; Zhang, Y.; Wang, T.; Kim, D.-Y.; Mei, J.; Marder, S. R.; Graham, K. R. Influence of dopant size and electron affinity on the electrical conductivity and thermoelectric properties of a series of conjugated polymers. *J. Mater. Chem. A* **2018**, *6*, 16495−16505.
(50) Wu, E. C.; Salamat, C. Z.; Ruiz, O. L.; Qu, T.; Kim, A.; Tolbert, S. H.; Schwartz, B. J. Counterion Control and the Spectral Signatures of Polarons, Coupled Polarons, and Bipolarons in Doped P3HT Films. *Adv. Funct. Mater.* **2023**, *33*, 2213652.
(51) Li, H.; Song, J.; Xiao, J.; Wu, L.; Katz, H.; Chen, L. Synergistically Improved Molecular Doping and Carrier Mobility by Copolymerization of Donor-Acceptor and Donor-Donor Building Blocks for Thermoelectric Application. *Adv. Funct. Mater.* **2020**, *30*, 2004378.
(52) Xu, J.; Wu, H.-C.; Mun, J.; Ning, R.; Wang, W.; Wang, G.-J. N.; Nikzad, S.; Yan, H.; Gu, X.; Luo, S.; Zhou, D.; Tok, J. B. H.; Bao, Z. Tuning Conjugated Polymer Chain Packing for Stretchable Semiconductors. *Adv. Mater.* **2022**, *34*, 2104747.
(53) Furlani, A.; Russo, M. V.; Polzonetti, G.; Martin, K.; Wang, H. H.; Ferraro, J. R. Spectroscopic Studies of FeCl3-Doped Polymers of Polyphenylacetylene. *Appl. Spectrosc.* **1990**, *44*, 331−334.
(54) Russo, M. V.; Polzonetti, G.; Furlani, A. XPS and IR investigations of FeCl3-doped polyphenylacetylene: the solvent effect. *Synth. Met.* **1991**, *39*, 291−301.
(55) Kang, Y. H.; Ko, S.-J.; Lee, M.-H.; Lee, Y. K.; Kim, B. J.; Cho, S. Y. Highly efficient and air stable thermoelectric devices of poly(3-hexylthiophene) by dual doping of Au metal precursors. *Nano Energy* **2021**, *82*, 105681.
(56) Lim, E.; Glaudell, A. M.; Miller, R.; Chabinyc, M. L. The Role of Ordering on the Thermoelectric Properties of Blends of Regioregular and Regiorandom Poly(3-hexylthiophene). *Adv. Electron. Mater.* **2019**, *5*, 1800915.
(57) Yang, C.-Y.; Jin, W.-L.; Wang, J.; Ding, Y.-F.; Nong, S.; Shi, K.; Lu, Y.; Dai, Y.-Z.; Zhuang, F.-D.; Lei, T.; Di, C.-A.; Zhu, D.; Wang, J.-Y.; Pei, J. Enhancing the n-Type Conductivity and Thermoelectric Performance of Donor-Acceptor Copolymers through Donor Engineering. *Adv. Mater.* **2018**, *30*, 1802850.
(58) Scheunemann, D.; Vijayakumar, V.; Zeng, H.; Durand, P.; Leclerc, N.; Brinkmann, M.; Kemerink, M. Rubbing and Drawing: Generic Ways to Improve the Thermoelectric Power Factor of Organic Semiconductors? *Adv. Electron. Mater.* **2020**, *6*, 2000218.
(59) Zapata-Arteaga, O.; Marina, S.; Zuo, G.; Xu, K.; Dörling, B.; Pérez, L. A.; Reparaz, J. S.; Martín, J.; Kemerink, M.; Campoy-Quiles, M. Design Rules for Polymer Blends with High Thermoelectric Performance. *Adv. Energy Mater.* **2022**, *12*, 2104076.
(60) Chen, A. X.; Kleinschmidt, A. T.; Choudhary, K.; Lipomi, D. J. Beyond Stretchability: Strength, Toughness, and Elastic Range in Semiconducting Polymers. *Chem. Mater.* **2020**, *32*, 7582−7601.

https://doi.org/10.1021/acsami.3c15651
ACS Appl. Mater. Interfaces 2024, 16, 3764−3777

(61) Wang, G.-J. N.; Gasperini, A.; Bao, Z. Stretchable Polymer Semiconductors for Plastic Electronics. *Adv. Electron. Mater.* **2018**, *4*, 1700429.
(62) Pei, D.; An, C.; Zhao, B.; Ge, M.; Wang, Z.; Dong, W.; Wang, C.; Deng, Y.; Song, D.; Ma, Z.; Han, Y.; Geng, Y. Polyurethane-Based Stretchable Semiconductor Nanofilms with High Intrinsic Recovery Similar to Conventional Elastomers. *ACS Appl. Mater. Interfaces* **2022**, *14*, 33806−33816.
(63) Wang, J.; Wang, Y.; Li, K.; Dai, X.; Zhang, L.; Wang, H. Lateral Fully Organic P-N Diodes Created in a Single Donor-Acceptor Copolymer. *Adv. Mater.* **2022**, *34*, 2106624.
(64) Zeng, Y.; Zheng, W.; Guo, Y.; Han, G.; Yi, Y. Doping mechanisms of N-DMBI-H for organic thermoelectrics: hydrogen removal vs. hydride transfer. *J. Mater. Chem. A* **2020**, *8*, 8323−8328.
(65) Huang, D.; Yao, H.; Cui, Y.; Zou, Y.; Zhang, F.; Wang, C.; Shen, H.; Jin, W.; Zhu, J.; Diao, Y.; Xu, W.; Di, C.-a.; Zhu, D. Conjugated-Backbone Effect of Organic Small Molecules for n-Type Thermoelectric Materials with ZT over 0.2. *J. Am. Chem. Soc.* **2017**, *139*, 13013−13023.

https://doi.org/10.1021/acsami.3c15651
ACS Appl. Mater. Interfaces 2024, 16, 3764−3777